**PAPER** • **OPEN ACCESS**

# Triple junction benchmark for multiphase-field models combining capillary and bulk driving forces

To cite this article: P W Hoffrogge *et al* 2025 *Modelling Simul. Mater. Sci. Eng.* **33** 015001

OPEN ACCESS
IOP Publishing
Modelling and Simulation in Materials Science and Engineering
Modelling Simul. Mater. Sci. Eng. **33** (2025) 015001 (29pp) https://doi.org/10.1088/1361-651X/ad8d6f

# Triple junction benchmark for multiphase-field models combining capillary and bulk driving forces

**P W Hoffrogge[1,2,*], S Daubner[2,3], D Schneider[1,2,3], B Nestler[1,2,3], B Zhou[4] and J Eiken[4]**

[1] Institute of Nanotechnology—Microstructure Simulations (INT-MS), Karlsruhe Institute of Technology, Hermann-von-Helmholtz-Platz 1, 76344 Eggenstein-Leopoldshafen, Germany
[2] Institute for Digital Materials Science (IDM), Karlsruhe University of Applied Sciences, Moltkestrasse 30, 76133 Karlsruhe, Germany
[3] Institute for Applied Materials (IAM-MMS), Karlsruhe Institute of Technology, Strasse am Forum 7, 76131 Karlsruhe, Germany
[4] Access e.V., Intzestraße 5, 52072 Aachen, Germany

E-mail: paul.hoffrogge@kit.edu

Received 28 May 2024; revised 5 October 2024
Accepted for publication 31 October 2024
Published 18 November 2024

**Abstract**

A benchmark problem is formulated which is well suited for the validation of mesoscopic phase-field models for grain-boundary migration in polycrystals. First, an analytical steady-state solution of the sharp moving boundary problem is derived for a symmetric lamellar structure, which is valid for arbitrary bulk driving forces and triple junction angles. Characteristic quantities are identified to reduce the parameter space which in turn allows a systematic comparison of simulations and analytical results. Various multiphase-field (MPF) formulations are compared which approximate the sharp interface problem in terms of a diffuse regularization. An interfacial thickness convergence study reveals that the model error is largely dependent on the ratio of bulk to interfacial stabilizing force as well as the underlying model formulation. An additional grid convergence study highlights the efficiency of a more advanced discretization scheme. The results can be used to guide the selection of appropriate

* Author to whom any correspondence should be addressed.

models and to estimate the interface thickness and spatial resolution required to achieve a given accuracy target. The post-processing framework consists of a fully automated determination of well-defined metrics from the phase field simulation data, eliminating human bias and facilitating reproducibility. The corresponding code is made openly available to assist the materials science and engineering community in validating MPF, multi-order parameter and similar model developments. We believe that this work provides a reliable benchmark procedure to better understand the potentials and limitations of current MPF models as well as alternative approaches.

Supplementary material for this article is available online

Keywords: phase-field modeling, benchmark, grain-boundary migration, capillarity

## 1. Introduction

The phase-field (PF) method is a versatile and established tool in materials science and engineering. Current models employing the multiphase-field (MPF) paradigm are capable of handling a large number of phases and grains [1–3]. Such multiphase and/or polycrystalline systems consist not only of grain and phase boundaries but also of triple and higher order junctions, where the balance of interfacial forces should hold [4]. This condition which is also known as Young's law [5] in 2D defines the dihedral angles at triple points (in 2D) or lines (in 3D) based on the interfacial energies of adjacent interfaces. Deviations from these equilibrium angles may be of physical origin, e.g. as a result of finite junction mobility [6–8] or line tension of the junctions [9, p 337 ff.]. Even though such effects may lead to an observable size effect in nanocrystalline samples [10], they can usually be neglected on the microscale. This stems from the fact that an interface can be regarded as a region with its own atomistic arrangement and a finite thickness [11, 12]. In the nanocrystalline case, it is clear that the importance of crystal defects (boundaries and junctions) increases relative to the grain size, since the length scales (grain diameter vs. interface/defect thickness) approach a comparable magnitude [13]. When modeling microstructural problems using PF approaches, the interfacial thickness is often artificially enlarged in order to reduce computational cost. Therefore, such effects may arise much earlier than physically expected (i.e. at the microscale) [14]. Interfacial-thickness dependent outcomes of a PF model are clearly undesirable and the removal of such spurious terms facilitates quantitative and cost-effective simulations [15]. Some approaches tremendously reduce the computational cost without compromising accuracy by tailoring the discretization of the model to the underlying grid [16–18]. Since these approaches allow for a much smaller interfacial width than conventional PF methods, it is expected that interface-thickness dependent effects can be significantly suppressed. In general, it would be desirable to benchmark various model formulations with respect to a sound and accurate reference or gold standard for well-defined geometries. Recent benchmarks [19, 20] address the case of grain-boundary (GB) migration subject to purely capillary forces with respect to a closed-form analytical solution of the GB geometry and velocity valid for arbitrary dihedral angles. A similar setup has been used by Staublin *et al* [21] for the validation of an orientation-field model. The analytical solution used in both works was first derived by Mullins [22] for the case of equal interfacial energies.

Additional bulk driving forces are often required to account for microstructural phenomena such as recrystallization [23], solidification [24] or martensitic phase transformations [25]. Large bulk driving forces can be challenging for PF models since they promote distortion of the interface which renders the model result inaccurate or even entirely meaningless. A working approach [25] based on an initial idea in [26] incorporates an additional stabilizing interfacial energy term which can reduce the distortion of the interface to a great extent. Very recently, an additional number of new model formulations has been presented to tackle the problem of large bulk driving forces [14, 27, 28].

The efficiency and accuracy of PF models subject to simultaneous bulk and capillary forces have mostly been evaluated for simple two-phase setups, see [16, figure 3] and [27, figure 5/6]. Polycrystalline benchmarks of GB migration employed in [27, 29, 30] are claimed to be generic, but are in fact based on simplifying assumptions. A more detailed discussion can be found in the works of Eiken [20] and Daubner *et al* [19]. Therefore, benchmarking PF approaches including bulk effects in a polycrystalline environment is currently prohibited due to the lack of an accurate reference solution.

To fill this gap, the present paper aims to provide an analytical solution for the case where an additional bulk driving force acts on the curved interface, thus facilitating the mutual comparison of existing models in terms of their accuracy and efficiency. For simplicity, the driving force is assumed to be constant in time and across the domain. The benchmark focuses on boundary migration according to rate-reaction theory [31], also known as attachment kinetics [32], which is mainly relevant for grain boundaries. It does not include the diffusion of heat or chemical species, which is commonly encountered at phase boundaries (e.g. liquid/solid interfaces). The benchmark consists of a steady-state solution that can be constructed for arbitrary dihedral angles and arbitrarily large bulk driving forces. Although the GB geometry and velocity cannot be given in a simple and accessible closed form, the implicit analytical solution only requires a single numerical integration step, which can be easily implemented in any programming language. We make the benchmark solution as well as the simulation postprocessing environment available as open source software [33] to promote the utilization of the benchmark in the materials science and engineering community.

## 2. Benchmark definition

As discussed in our previous work [19], a triple junction is well-suited to benchmark MPF and multi-order parameter models. It contains all the model complexity, which arises when formulating a multiphase extension to a two-phase problem while the initial and boundary conditions are sufficiently simple. Furthermore, such a benchmark is also a suitable reference for orientation-field models [21].

The initial setup is given by a rectangular domain containing three grains, each distinguished by an order parameter, as sketched in figure 1. The width of the domain $W$ is given in table 1, while the height $H$ needs to be adjusted depending on the simulation input parameters. The simulation domain must be high enough to ensure convergence of the grain boundary motion towards a steady state, which depends on the interfacial energy ratio $\gamma_{\alpha\beta}/\gamma_0$ and the driving force $\Delta f$. All boundaries are subject to insulating (Zero-Neumann) boundary conditions which reflects mirror symmetry on the left and right boundaries, i.e. an infinite domain of alternating $\alpha$ and $\beta$ lamellae.

The physical input parameters are chosen in the order of magnitude for typical microstructure simulations of aluminum [9] as listed in table 1. Please note that numerical input parameters of the solver may conveniently be set employing a unit system with 1 ms as the time

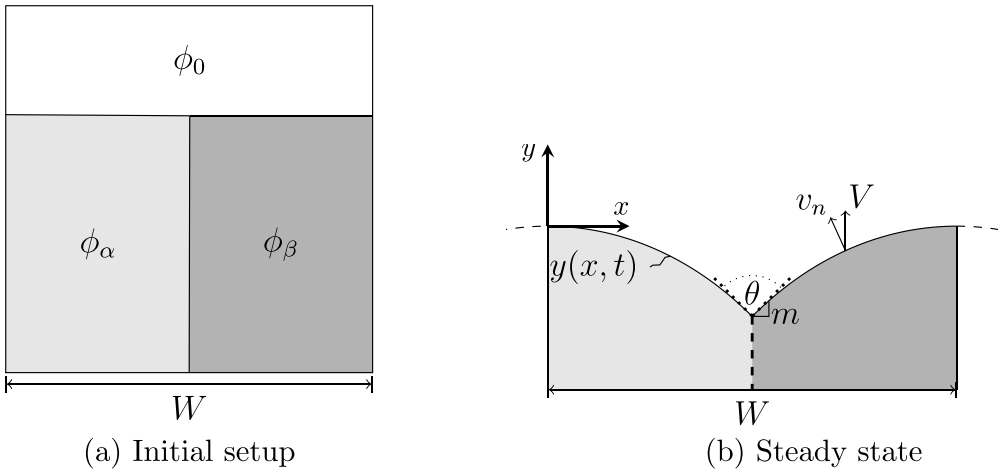


**Figure 1.** Sketch of the triple junction in (a) the initial problem setup and (b) a steady-state configuration. In the steady state the coordinate system moves in vertical direction with a constant velocity $V$. This coordinate system is used for numerical evaluation in section 6.

**Table 1.** Set of physical input parameters in a typical range for aluminum.

| Parameter | Symbol | Value | Unit |
|---|---|---|---|
| Width of domain | $W$ | 50 | $\mu$m |
| Interfacial energy | $\gamma_{\alpha 0} = \gamma_{\beta 0} = \gamma_0$ | 0.5 [a] | J m$^{-2}$ |
| | $\gamma_{\alpha\beta}$ | $[\sqrt{3}\gamma_0, \gamma_0]$ | J m$^{-2}$ |
| Mobility | $M_{\alpha 0} = M_{\beta 0} = M_0$ | $2 \times 10^{-8}$ [b] | m$^4$ (J s)$^{-1}$ |
| | $M_{\alpha\beta}$ | $2 \times 10^{-8}$ | m$^4$ (J s)$^{-1}$ |
| Driving force | $\Delta f$ | $\pm[0, 0.01, \ldots, 1]$ [c] | MPa |

[a] Estimated from [9, figure 2.4],
[b] Estimated from [9, figure 3.61],
[c] Taken from [9, table 3.1].

unit, 1 $\mu$m as the length unit and 1 pJ as the energy unit. This ensures that all input parameters are within few orders of unity for numerical reasons.

## 3. Analytical considerations

### *3.1. Characteristic quantities*

*3.1.1. Relation of capillary and bulk driving forces.* In general, a good qualitative understanding of the role of capillary and bulk driving forces is essential to estimate their relative importance. It is necessary to discuss regimes of small and large bulk driving forces by introducing characteristic nondimensional quantities that relate capillary and bulk driving forces in an order-of-magnitude sense, just like the well-known Reynolds number which estimates the relation of inertia to friction forces in a fluid.

The first characteristic quantity

$$\tilde{p} \equiv \frac{W}{\gamma_0}\Delta f \tag{1}$$

stems from the domain size[5], i.e. the length scale which controls the order-of-magnitude variation in the grain boundary geometry. It relates the bulk driving force $\Delta f$ to the capillary driving force $\kappa\gamma_0$ where the curvature $\kappa$ scales with the inverse width of the domain $\kappa \propto 1/W$.

Herewith, we define the following regimes

| | |
|---|---|
| $\lvert\tilde{p}\rvert < 1$ | 'small driving forces' |
| $1 \leqslant \lvert\tilde{p}\rvert < 10$ | 'intermediate driving forces' |
| $\lvert\tilde{p}\rvert \geqslant 10$ | 'large driving forces'. |

The values listed in table 1 result in ratios $\tilde{p} = \pm[0, 1, \ldots, 100]$ and thus cover the complete range from small to large driving forces.

*3.1.2. Relation of interface-stabilizing and bulk driving forces.* For PF models, an additional length scale corresponds to the diffuse interface thickness. In the light of the previous characteristic number, we replace $W$ by the interfacial thickness $\eta$ to derive the dimensionless quantity

$$\tilde{p}_{\mathrm{PF}} \equiv \frac{\eta}{\gamma_0}\Delta f. \tag{2}$$

This last expression can be interpreted as the ratio of the bulk driving force to the interface stabilizing force (the well/obstacle potential scales with $\gamma_0/\eta$). In general, the interfacial thickness should be much smaller than the domain size, and thus, we obtain $|\tilde{p}_{\mathrm{PF}}| < |\tilde{p}|$. Therefore, the bulk driving force can only be large with respect to the interface stabilizing force when we are far in the large driving force regime.

*3.1.3. Characteristic timescales.* The analytical derivation assumes a steady state, but the simulation starts with a T-shaped setup which will generally deviate from the steady-state solution. Therefore, the moving grain boundary should be given sufficient time to reach a time-invariant shape. The period of time during which the GB smoothly approaches the shape of the steady state is commonly referred to as the transient regime. To quantify this, we consider the time

$$t_{\mathrm{transient}} = \frac{W^2}{M_{\mathrm{GB}}\gamma_0} \tag{3}$$

in order to derive a dimensionless time as $\tilde{t} = t/t_{\mathrm{transient}}$. We expect that the steady state is reached when $\tilde{t}$ is sufficiently large with respect to unity.

In terms of the PF method, another time scale can be defined by replacing $W$ by $\eta$

$$t_{\mathrm{PF}} = \frac{\eta^2}{M_{\mathrm{GB}}\gamma_0} \tag{4}$$

[5] For an arbitrary polycrystal, we may replace $W$ by the average grain size.

which can be interpreted as the time scale for forming the diffuse PF profile. Since $\eta \ll W$, this time is much shorter than the transient, i.e.

$$\frac{t_{\mathrm{PF}}}{t_{\mathrm{transient}}} = \left(\frac{\eta}{W}\right)^2 \ll 1\,.$$

Accordingly, choosing $\tilde{t}$ large enough should be a sufficient condition for the interfacial profile to be constant in time.

*3.1.4. Relation of interfacial energies.* An additional characteristic quantity is defined by the ratio of the GB energies between the stationary (i.e. vertically aligned) grain boundary and the moving curved GB. The ratio of the two grain boundary energies is a dimensionless quantity

$$\tilde{\gamma} = \frac{\gamma_{\alpha\beta}}{\gamma_0}\,. \tag{5}$$

According to Young's law, the dihedral angle is directly related to this ratio [19, equation (29)]

$$\theta = 2\arccos\left(\frac{\tilde{\gamma}}{2}\right). \tag{6}$$

Therefore, a small ratio $\tilde{\gamma}$ should result in a relatively flat GB geometry, whereas a high ratio leads to a steep GB profile. Moreover, only ratios below $\tilde{\gamma} = 2$ are meaningful, since $\theta$ tends to zero for this limit, corresponding to an infinitely steep GB profile.

*3.1.5. Grid and interface resolution.* For a uniform grid, the grid spacings $\Delta x$ and $\Delta y$ are defined as the distance between two grid nodes in each direction (units of length). In the current document, both dimensions are equally spaced, i.e. $\Delta x = \Delta y$. A dimensionless quantity is the number of grid points in each direction given by $N_x = W/\Delta x$, $N_y = H/\Delta x$ where $H$ is the height of the domain. In order to resolve the thin interface thickness in PF models, a sufficient number of grid points in the interface is needed. Therefore, the quantity

$$n_{\mathrm{int}} \equiv \frac{\eta}{\Delta x} \tag{7}$$

is introduced, relating the interface thickness parameter $\eta$ to the grid spacing. This quantity is the number of grid points occupied by an equilibrium sinusoidal interface.

### *3.2. Sharp-interface solution*

*3.2.1. Problem formulation.* Rate-reaction theory [31, 32] relates the interface normal velocity $v_n$ to a driving force. In the current setup we consider the superposition of two effects: A capillary driving force resulting from an isotropic GB energy $\gamma_0$ and a constant bulk driving force $\Delta f$. This leads to the equation

$$v_n = M_{\mathrm{GB}}\left(\Delta f - \gamma_0 \kappa\right) \tag{8}$$

where $M_{\mathrm{GB}}$ is the constant mobility of the grain boundary and $\kappa$ its curvature.

A curved grain boundary as sketched in figure 1(b) is given by the function $y(x,t)$ in a Cartesian coordinate system where $x$ and $y$ are the horizontal and vertical coordinate, respectively. It is assumed that the GB moves vertically with a constant velocity $V \equiv \partial y(x,t)/\partial t$. This can be expressed more formally as

$$y(x,t) \equiv y(x) + y_0(t) \tag{9}$$

$$V = y_0'(t) \tag{10}$$

where $[x = 0, y = y_0(t)]$ is the location of the grain boundary at the mirror plane. $y_0(t)$ is a linear function in time and $y(x)$ is a univariate function representing the geometry of the GB in the moving frame of reference. In contrast to our recent paper [19], $V$ is positive if the motion is upwards. The GB's curvature can be expressed in terms of first and second derivatives as

$$\kappa = -\frac{y''(x)}{\left(1 + (y'(x))^2\right)^{3/2}}. \tag{11}$$

Since the normal velocity is given by

$$V = v_n \sqrt{1 + (y'(x))^2}, \tag{12}$$

the following nonlinear ordinary differential equation for $y$

$$y''(x) = \frac{V}{M_{\mathrm{GB}}\gamma_0}\left(1 + (y'(x))^2\right) - \frac{\Delta f}{\gamma_0}\left(1 + (y'(x))^2\right)^{3/2} \tag{13}$$

is obtained which is subject to the following boundary conditions

$$y(0) = 0, \quad y'(0) = 0, \quad y'(W/2) = -m.$$

The first condition fixes the location of the GB at the mirror plane, the second condition ensures the mirror symmetry and the last condition enforces the triple-junction slope $m$. Note that the geometry is only determined for the left-hand side of figure 1(b) (i.e. for $x \leqslant W/2$). The right-hand side can be determined from the symmetry constraint as $y(x,t) = y(W-x,t)\,\forall x > W/2$. The triple-junction slope $m$ is related to the interfacial energy ratio $\tilde{\gamma}$ by Young's law [13, equation (127)] and is geometrically related to the dihedral angle $\theta$ (cf figure 1(b))

$$m = \frac{\tilde{\gamma}}{\sqrt{4 - \tilde{\gamma}^2}} = \cot\left(\frac{\theta}{2}\right). \tag{14}$$

In the following, we start with certain limiting cases to gain some understanding of the problem before solving it thoroughly.

*3.2.2. Stationary grain boundary.* For the special case of a stationary interface ($v_n = 0$), equation (8) yields the condition that the curvature is a constant equal to

$$\kappa = \frac{\Delta f}{\gamma_0}. \tag{15}$$

This means that the GB geometry is a circular arc (see figure 2(b)). In order to satisfy the boundary conditions, it is possible to derive the picked value of $\kappa$ by a graphical construction:

Draw an arc with its maximum located at the origin and fulfilling the dihedral angle $\theta$ at $x = W/2$. This gives

$$\kappa = \frac{1}{R} = \frac{2\cos\left(\frac{\theta}{2}\right)}{W} = \frac{\tilde{\gamma}}{W} \tag{16}$$

where $R$ is the radius of the arc. Using the relation between the curvature and driving force from equation (15), we find that the stationary case can only be satisfied for a certain (dimensionless) driving force that equals the ratio of the interfacial energies

$$\tilde{p} = \tilde{\gamma} = \frac{2m}{\sqrt{1+m^2}}. \tag{17}$$

Figuratively speaking, this is the driving force 'pushing the GB up' which is balanced by the capillary driving force pointing downwards, so that the GB stops moving.

*3.2.3. Large bulk driving force limits.* The solution for vanishing driving forces has already been presented in [19] while in this context the behavior of the solution for large bulk driving forces is of particular interest. Inspecting equation (8) for large $|\Delta f|$ (or $\gamma_0 \to 0$, more precisely $|\tilde{p}| \to \infty$), it is expected that the curvature term on the right-hand side can be neglected. This yields

$$\frac{V}{\sqrt{1+(y'(x))^2}} \approx \Delta f. \tag{18}$$

Since $V$ and $\Delta f$ are constant, the only possibility to balance left- and right-hand side for every $x$ is that $|y'(x)|$ approaches to a constant in the large-driving force limit. This corresponds to a (piecewise) planar GB geometry. We expect two possibilities:

(i) The GB tends to a hat shape, as shown in figure 2(a): $|y'(x)| \to m$. This fulfills the triple-junction boundary conditions but violates the symmetry condition. This implies $V/(M_{\mathrm{GB}}\Delta f) \to \sqrt{1+m^2}$ as $|\tilde{p}| \to \infty$.
(ii) The GB tends to a horizontal plane, as shown in figure 2(c): $|y'(x)| \to 0$ which would fulfill the symmetry condition $y'(0) = 0$ but violate the boundary condition at the triple junction. This implies $V/(M_{\mathrm{GB}}\Delta f) \to 1$ as $|\tilde{p}| \to \infty$.

In the first case, the symmetry could be recovered by a thin boundary layer near the center $x = 0$ which regularizes the problem. In the second case, it is likely that the curvature term leads to a boundary layer near $x = W/2$ which becomes thinner as $|\Delta f|$ increases in order to comply with the boundary condition.

For the hat case, the limiting tip curvature $\kappa_{\mathrm{tip}} = \kappa(x = 0)$ is calculated by inserting $V/(M_{\mathrm{GB}}\Delta f) = \sqrt{1+m^2}$ and $y'(0) = 0$ into equation (8). This gives

$$\kappa_{\mathrm{tip}} = \frac{1}{R_{\mathrm{tip}}} = \frac{\Delta f}{\gamma_0}\left(1 - \sqrt{1+m^2}\right). \tag{19}$$

This equation reveals an increasing sharpness of the tip with the magnitude of the driving force and a discontinuity of the first derivative is reached in the limiting case. Similarly, for the

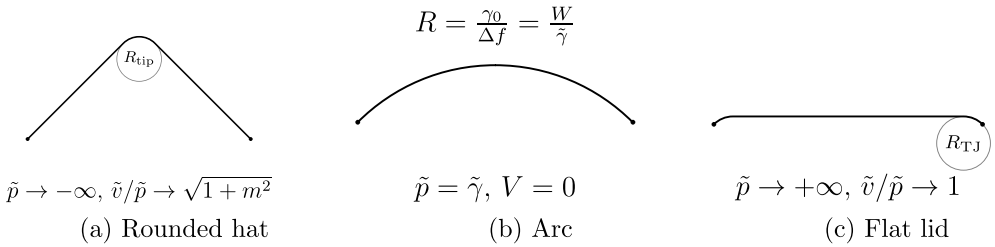


(a) Rounded hat (b) Arc (c) Flat lid

**Figure 2.** Schematic depiction of the limiting grain-boundary geometries where the dimensionless driving force $\tilde{p} = \Delta f W/\gamma_0$ increases from left to right.

horizontal case, we calculate the limiting curvature $\kappa_{\mathrm{TJ}}$ at the triple junction where $|y'(1/2)| = m$. This gives a similar relation

$$\kappa_{\mathrm{TJ}} = \frac{1}{R_{\mathrm{TJ}}} = \frac{\Delta f}{\gamma_0}\frac{\sqrt{1+m^2}-1}{\sqrt{1+m^2}}\,. \tag{20}$$

Informally, for the hat shape, the tip curvature should 'glue' the two linear segments with slope $\pm m$ together. For the lid-like shape, the GB near the triple junction needs to bend toward horizontal alignment (i.e. become more flat). Accordingly, in both cases we expect positive curvatures in order to ensure compatibility with the behavior far away from the tip or the triple junction. Thus, it is expected that the hat shape is the limiting shape for $\tilde{p} \to -\infty$ and the horizontal plane is the limiting shape for $\tilde{p} \to +\infty$. The corresponding regularized shapes are shown schematically in figure 2.

#### *3.2.4. General solution.*

*Non-dimensionalization.* To simplify the derivation, the dimensionless coordinates $\tilde{x}, \tilde{y}$ and the dimensionless velocity $\tilde{v}$ are introduced as

$$\tilde{x} \equiv \frac{x}{W}, \quad \tilde{y} \equiv \frac{y}{W}, \quad \tilde{v} \equiv \frac{VW}{M_{\mathrm{GB}}\gamma_0}\,.$$

This gives the following problem

$$\tilde{y}''(\tilde{x}) = \tilde{v}\left(1+(\tilde{y}'(\tilde{x}))^2\right) - \tilde{p}\left(1+(\tilde{y}'(\tilde{x}))^2\right)^{3/2} \tag{21}$$

$$\tilde{y}(0) = 0 \tag{22}$$

$$\tilde{y}'(0) = 0 \tag{23}$$

$$\tilde{y}'(1/2) = -m\,, \tag{24}$$

which reduces the dimensionality of the variable set from six ($V$, $W$, $M_{\mathrm{GB}}$, $\Delta f$, $\gamma_{\alpha\beta}$, $\gamma_0$) to three ($\tilde{v}$, $\tilde{p}$, $\tilde{\gamma}$). We expect that $\tilde{v}$ and $\tilde{p}$ are not independent since a larger driving force should result in an acceleration of the grain boundary. Therefore, we may consider $\tilde{p}$ as the independent and $\tilde{v}$ as the dependent parameter.

*GB velocity.* Our goal is to solve equation (21) to determine the unknown relation between velocity and driving force $\tilde{v}(\tilde{p})$ together with the GB geometry. The detailed solution procedure is presented in appendix A. The solution for the velocity is given in an implicit form based on the relation $q \equiv \tilde{v}/\tilde{p}$ and reads

$$\tilde{v} = 2\left(\frac{\arctan\left(\frac{mq}{\sqrt{1+m^2}\sqrt{1-q^2}}\right) + \arctan\left(\frac{m}{\sqrt{1-q^2}}\right)}{\sqrt{1-q^2}} - \arctan(m)\right). \tag{25}$$

The velocity can be obtained for values of $\tilde{p}$ through a root-finding algorithm. This method is implemented in the Supplemental Python code [33]. Equation (25) is ill-defined for certain values of $q$. These singular cases are given in table A1 which also includes the case of a vanishing driving force as described in [19].

*GB geometry.* The analytical solution of the GB geometry is given by

$$\tilde{x} = \frac{1}{q\tilde{p}}\left(\arctan(s) + \frac{\operatorname{arctanh}\left(\frac{sq}{\sqrt{1+s^2}\sqrt{q^2-1}}\right) + \operatorname{arctanh}\left(\frac{s}{\sqrt{q^2-1}}\right)}{\sqrt{q^2-1}}\right) \tag{26}$$

where the slope $s \equiv y'(x) = \tilde{y}'(\tilde{x})$ is a parameter within the interval $-m \leqslant s \leqslant m$. This formula can be graphically inverted to obtain $\tilde{y}'(\tilde{x})$ in the interval $-1/2 < \tilde{x} < 1/2$. Numerical integration subject to the BCs from equation (22) then yields the final solution $\tilde{y}(\tilde{x})$. For $q = 0$ and $q = -1$, the above formula is undefined. We use L'Hospital rule to determine the following limiting cases

$$\lim_{q\to 0}\tilde{x} = -\frac{s}{\tilde{p}\sqrt{1+s^2}}, \quad \lim_{q\to -1}\tilde{x} = \frac{1}{\tilde{p}}\left(\frac{\sqrt{1+s^2}-1}{s} - \arctan(s)\right).$$

which completes the analytical treatment.

The GB geometry is shown for various driving forces in figure 3(a) which essentially matches the expected behavior from figure 2. The dependence of the interface velocity on the driving force is illustrated in figure 3(b) for three different dihedral angles together with the corresponding large-driving force limits. It can be seen that the large-$\Delta f$ limiting behavior is very well established for $|\tilde{p}| \geqslant 5$. For small driving forces, a linear approximation can be applied to the interface velocity as $\tilde{v} \approx \tilde{v}_0 + \tilde{p}\tilde{v}_1$ with $\tilde{v}_0 = \theta - \pi$ and $\tilde{v}_1 = 2\operatorname{arctanh}(\cos(\theta/2))/(\pi - \theta)$ (more details given in the supplementary material).

## 4. Benchmark simulations

The triple junction benchmark described above can be used to quantitatively validate and compare the accuracy of mesoscopic PF models that approximate the moving boundary problem of a singular surface by a diffuse representation. In such models, the interface width becomes a numerical parameter, while the capillary forces should be accurately described in relation to the bulk driving force. Note that the benchmark is equally applicable to other numerical approaches that solve the given sharp interface problem such as multi-order parameter models, level-set methods, et cetera. Within the scope of this work, we use a common multiphase

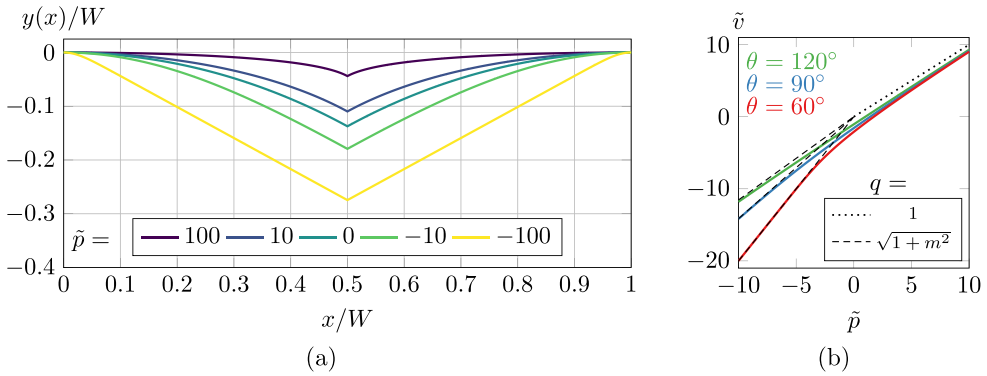


**Figure 3.** Sharp interface solution. (a) Grain-boundary geometry for $\theta = 120°$ (i.e. $\tilde{\gamma} = 1$) at varying driving forces and (b) dimensionless grain-boundary velocity as a function of the dimensionless driving force for three different dihedral angles together with the derived limiting cases (cf figure 2).

field concept and demonstrate how the benchmark can be applied to quantitatively validate the accuracy of alternative model variations and implementations over a wide range of bulk driving forces and numerical resolutions.

### *4.1. The multi-phase field formulation*

The basic multi-phase field formulation is adopted from [3], where the spatial arrangement of multiple phases or grains is described by multiple PF variables $\phi_\alpha(\boldsymbol{x},t), \alpha \in \{1,\dots,N\}$. Their values are equal to unity in the bulk of the corresponding phase (grain) and continuously change to zero over diffuse interface regions. The collection of order parameters fulfills the unity sum constraint $\sum_{\alpha=1}^{N} \phi_\alpha = 1$ everywhere in space. Bulk and interfacial contributions in the free energy functional are decoupled so that the interfacial thickness $\eta$ can be adjusted for computational convenience. Application of a multiphase relaxation approach under consideration of the unity sum constraint yields the set of PF equations:

$$\frac{\partial \phi_\alpha}{\partial t} = \sum_{\beta \neq \alpha}^{\tilde{N}} M_{\alpha\beta} \left[ b_{\alpha\beta} \Delta f_{\alpha\beta} - \gamma_{\alpha\beta} K_{\alpha\beta} + J_{\alpha\beta} \right]. \tag{27}$$

The present notation is chosen so that the definition of the interfacial mobility $M_{\alpha\beta}$, the interfacial energy $\gamma_{\alpha\beta}$ and the driving force $\Delta f_{\alpha\beta}$ match those in the sharp interface solution in equation (8) and the corresponding data in table 1. The term $K_{\alpha\beta}$ accounts for curvature and implicitly stabilizes the diffuse interface profile, while $J_{\alpha\beta}$ accounts for additional junction forces. Both terms are derived from a gradient term ($\propto \boldsymbol{\nabla}\phi_\alpha \cdot \boldsymbol{\nabla}\phi_\beta$) in combination with a multi-obstacle potential ($\propto \phi_\alpha \phi_\beta$):

$$K_{\alpha\beta} = \frac{1}{\tilde{N}} \left[ \nabla^2 \phi_\beta - \nabla^2 \phi_\alpha + \frac{\pi^2}{\eta^2} (\phi_\beta - \phi_\alpha) \right], \tag{28}$$

$$J_{\alpha\beta} = \frac{1}{\tilde{N}} \sum_{\gamma \neq \beta \neq \alpha}^{N} (\gamma_{\beta\gamma} - \gamma_{\alpha\gamma}) \left( \nabla^2 \phi_\gamma + \frac{\pi^2}{\eta^2} \phi_\gamma \right). \tag{29}$$

A comparison of different interfacial formulations can be found in [19]. A special feature of the multi-obstacle formulations is that only contributions of locally interacting phases are considered. The amount of active phases $\tilde{N}$ appears as a denominator in equations (28) and (29) to account for identical phase contributions from superimposed interactions. Adopting the notation of [14, 34], $\tilde{N}^{-1}$ is not directly multiplied with the mobility which allows for a decoupled definition of the prefactor to the bulk driving force $b_{\alpha\beta}$.

### 4.2. The bulk driving force prefactor

Special emphasis shall be on the factor $b_{\alpha\beta}$ which can be used to distribute the bulk driving force along the diffuse interface under the constraint that the integral across the interface remains unchanged. This is important to minimize the distortion of the moving diffuse interface profile in mesoscopic models with a finite numerical interface thickness. Direct matching of the PF equation (equation (27)) to the sharp interface solution (equation (8)) reveals that the two-phase traveling wave solution is not distorted for $b_{\alpha\beta} = |\boldsymbol{\nabla}\phi_\alpha| = |\boldsymbol{\nabla}\phi_\beta|$. An open question is how to define the scaling factor $b_{\alpha\beta}$ in multi-phase regions. A detailed discussion of this subject can be found in [14]. In the context of this work, three different variants will be compared:

$$b_{\alpha\beta} = \begin{cases} \dfrac{\pi}{\eta}\sqrt{\phi_\alpha\phi_\beta} & \rightarrow B0 \\ \dfrac{2\pi}{\tilde{N}\eta}\sqrt{\phi_\alpha\phi_\beta} & \rightarrow B1 \\ \dfrac{\pi}{\eta}\left(\phi_\alpha+\phi_\beta\right)\sqrt{\phi_\alpha\phi_\beta} & \rightarrow B2. \end{cases} \tag{30}$$

Note that in two-phase regions, all three variants $B0$-$B2$ reduce to $\pi/\eta\sqrt{\phi_\alpha(1-\phi_\alpha)}$ which is the analytical expression of $|\boldsymbol{\nabla}\phi_\alpha|$ for the sinusoidal traveling wave solution. The first multiphase variant $B0$ simply equals the two-phase expression. The second variant $B1$ which adopts the multiphase scaling $(2/\tilde{N})$ from interfacial contributions has been used by Kubendran Amos *et al* [35]. The last variant $B2$, used e.g. in [34, 36, 37], refers to the one implemented in MICRESS since 2010, replacing the former variant B0.

### 4.3. Prefactors derived from interpolation functions

Alternatively, the weighting of the bulk driving force can be derived in a fully variational way from different interpolation functions in the bulk free energy $f_{\text{bulk}} = \sum_\alpha f^\alpha h^\alpha(\boldsymbol{\phi})$ which yields three alternative model formulations $H0$-$H2$. Using the relaxation ansatz by [38] the following set of PF equations is obtained:

$$\frac{\partial\phi_\alpha}{\partial t} = \sum_{\beta\neq\alpha}^{\tilde{N}} M_{\alpha\beta}\left[\frac{\pi^2}{4\tilde{N}\eta}\left(\frac{\partial f_{\text{bulk}}}{\partial\phi_\beta}-\frac{\partial f_{\text{bulk}}}{\partial\phi_\alpha}\right)-\gamma_{\alpha\beta}K_{\alpha\beta}+J_{\alpha\beta}\right] \tag{31}$$

which is almost identical to equation (27) but the term $b_{\alpha\beta}\,\Delta f_{\alpha\beta}$ has been replaced. Commonly used interpolation functions $h^\alpha = h(\phi_\alpha)/(\sum_\beta h(\phi_\beta))$ are normalized based on the numerator

$$h(\phi_\alpha) = \begin{cases} \phi_\alpha & \rightarrow H0 \\ \phi_\alpha^2\left(3-2\phi_\alpha\right) & \rightarrow H1 \\ \phi_\alpha^3\left(6\phi_\alpha^2-15\phi_\alpha+10\right) & \rightarrow H2 \end{cases}$$

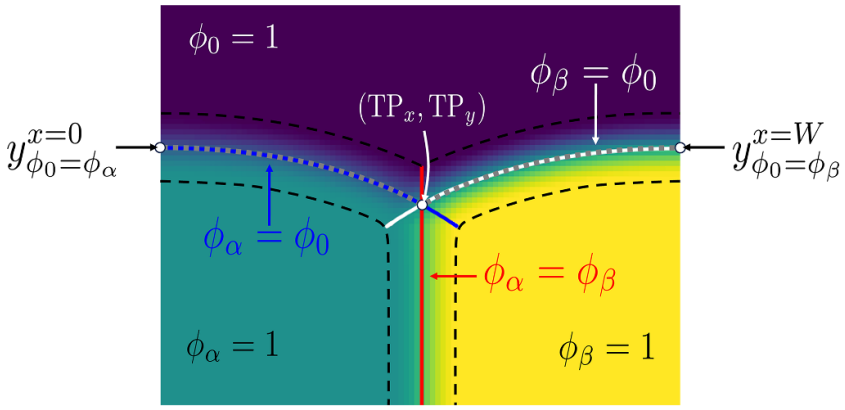


**Figure 4.** Exemplary triple junction in a diffuse representation with corresponding isolines between the phase-fields. The gray dotted line corresponds to the extracted grain boundary profile.

and ensure $\sum h^\alpha(\boldsymbol{\phi}) = 1$ throughout the domain. Note that due to this normalization, the bulk term $\partial f_{\mathrm{bulk}}/\partial\phi_\alpha = f^\alpha h'(\phi_\alpha)/\sum_\beta h(\phi_\beta) - h'(\phi_\alpha)/h^2(\phi_\alpha)\sum_\beta f^\beta h(\phi_\beta)$ contains contributions from all driving forces $f^\alpha, \ldots f^N$ for higher polynoms (i.e. *H*1 and *H*2).

### *4.4. Numerical implementation and automated parameter variation*

In the following sections, two different codes are employed (a) the software PACE3D [39] and (b) the commercial software MICRESS (V7.250). Both implementations are based on similar MPF formulations solved on finite difference stencils on equidistant grids with spacing $\Delta x$ and explicit time stepping. The commercial software MICRESS is based on model formulation *B*2 and comes with an additional grid correction scheme [16] (see section 6.3). To enable model comparison, all formulations *B*0-*B*2 and *H*0-*H*2 were implemented in PACE3D. The execution of benchmark simulations has been automated and, additionally, a metadata *.json* file is generated containing model parameters and numerical resolution information for each simulation. This allows for fully automated post-processing with the supplementary code [33]. This workflow approach is generic in the sense that it could easily be adapted to similar models such as multi-order parameter approaches. Once the code interface to another simulation software tool is defined, the workflows can be used in a fully automated manner.

## 5. Post-processing framework

To compare the simulation results to the analytical solution of the grain boundary velocity (equation (25)) and profile (equation (26)), we need to retrieve the sharp interface solution from the PF results. Therefore, pairwise isolines of PF variables are extracted where $\phi_\alpha = \phi_\beta$, $\phi_\alpha = \phi_0$ and, accordingly, $\phi_\beta = \phi_0$. The coordinates of the triple point ($\mathrm{TP}_x$, $\mathrm{TP}_y$) are then given by the intersection of pairwise isolines as shown in figure 4 and, thus, the simulated grain boundary profile is given by the gray dotted line which combines the isoline given by $\phi_\alpha = \phi_0$ (blue line) left of the triple point and $\phi_\beta = \phi_0$ (white line) to the right. The described procedure is implemented as a function on regular grids in the supplemental code [33] which is openly available on github.

For quantitative comparison of simulation studies with regard to the analytical solution, we define the following metrics:

(i) The **velocity** can be measured as the temporal change of

- the $y$-coordinate of the grain boundary profile at the domain boundary
  $V_{\text{left}} = [(y^{x=0}_{\phi_0=\phi_\alpha})^n - (y^{x=0}_{\phi_0=\phi_\alpha})^{n-1}]/\Delta t$,
  $V_{\text{right}} = [(y^{x=W}_{\phi_0=\phi_\alpha})^n - (y^{x=W}_{\phi_0=\phi_\alpha})^{n-1}]/\Delta t$;
- the $y$-coordinate of the triple point $V_{\text{TP}} = [(\text{TP}_y)^n - (\text{TP}_y)^{n-1}]/\Delta t$;
- the phase fraction of $\phi_0$ as $V_{\text{phase}} = -[(\int \phi_0 \text{d}V)^n - (\int \phi_0 \text{d}V)^{n-1}]/(W\Delta t)$;

Note that the velocities are defined along the $y$-direction as indicated in figure 1(b).

(ii) The **(mis-)match of numerical results for the grain boundary geometry** with regard to the analytical solution is quantified by a relative error measure introduced by the $L^2$-norm as
$\text{L2} = \sqrt{\int_0^1 (\tilde{y}^{\text{numeric}}(\tilde{x}) - \tilde{y}^{\text{analytic}}(\tilde{x}))^2 \text{d}\tilde{x} / \int_0^1 (\tilde{y}^{\text{analytic}}(\tilde{x}))^2 \text{d}\tilde{x}}$.
We numerically perform the integrals using composite trapezoidal rule on the discrete $\tilde{x}$-locations of the isoline representation $\tilde{y}^{\text{numeric}}$. In order to compare the analytical and numerical GB geometry in the same moving frame of reference, the maximum of the $\tilde{y}$-curve is set to zero, i.e. $\max(\tilde{y}^{\text{numeric}}) = 0$ is enforced.

The dihedral angle $\theta$ at the triple junction is not used as a metric for model evaluation as the computation is non-trivial and large errors can arise from the numerical evaluation of the angle. Schemes that assume linear segments in the triple phase region [40] depend on grid resolution and on the model parameters which define the diffuse interface width. Arc-fitting procedures [29, 41] are based on the assumptions that the GB geometry can be described by a circular arc which does not cover the general range of GB profiles as sketched in figure 2.

The evaluation procedure for a single simulation is illustrated in figure 5. The simulation is based on the values given in table 1, a numerical discretization with 100 cells along the $x$-direction, 10 grid points within the diffuse interface and a non-dimensional driving force of $\tilde{p} = 10$. The simulation was carried out using explicit time-stepping until a final time of $t_{\text{end}} = t_{\text{transient}}$ according to equation (3) was reached. From the velocity plot in figure 5(a), it becomes obvious that the various methods to measure velocity exhibit different convergence behaviors. The triple point velocity shows strong oscillations which can, in this case, be traced back to the obstacle potential and numerical errors which arise from the calculation of the triple point. The velocities $v_{\text{left}}$ and $v_{\text{right}}$ show the same convergence and much less oscillations. The magnified view in figure 5(b) reveals that even after the transient regime, oscillations persist as a result of the obstacle potential. The velocity value which is calculated based on the phase fractions $v_{\text{phase}}$ shows the smoothest behavior due to area integration. Minor oscillations still persist.

Due to the oscillating behavior, it is not straight forward to define an absolute or relative measure of convergence. For this reason, we decided to determine the mean value plus standard deviation over the time period from $t_{\text{transient}}/2$ until $t_{\text{transient}}$ which is exemplarily shown in figure 5(b). The green background color marks the time interval of averaging, the blue line is the mean value of $v_{\text{left}}$, while the blue shaded area illustrates the standard deviation. Similarly, the red line is the mean value of $v_{\text{phase}}$. Note that although $v_{\text{phase}}$ has a smaller standard deviation, this metric is more susceptible to the formation of spurious phases, i.e. both $v_{\text{left}}$ and $v_{\text{phase}}$ should be evaluated.

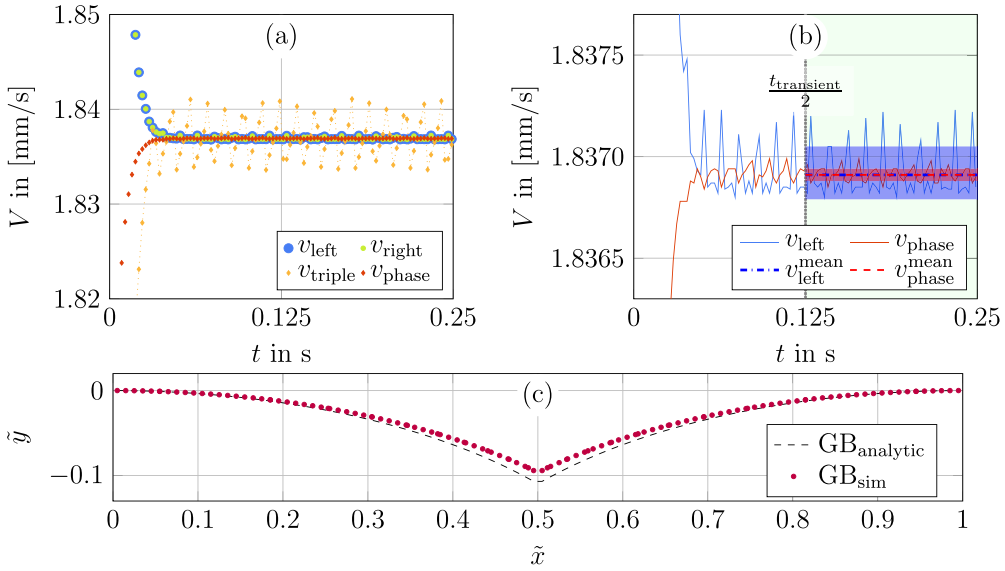


**Figure 5.** Evaluation of example simulation. (a) Velocity of grain boundary measured with methods introduced in section 5. (b) magnified view of oscillations in the numerically obtained velocities and averaging procedure in the steady-state regime, (c) numerically extracted final grain boundary profile in comparison with analytic solution.

Figure 5(c) shows the extracted grain boundary profile in the non-dimensional $(\tilde{x},\tilde{y})$ coordinate system. The L2 measure quantifies the mismatch of the analytic and simulated grain boundary profile. In the following, only the steady-state values defined above by the mean averaging over the time interval $t_{\text{end}} = t_{\text{transient}}$ will be plotted for various model formulations and over a range of driving forces. We apply the same procedure to compute the mean and standard deviation for the L2 norm, to average oscillations arising from the calculation of the triple point.

In the following, we illustrate the numerical evaluation procedure of the benchmark, firstly by performing convergence studies according to common phase field practice, and secondly by comparing some common model formulations.

## 6. Simulation results

### *6.1. Convergence toward sharp interface*

For meso-scopic length scales, the PF approach yields a diffuse representation of a sharp interface problem which leads to a model-intrinsic dependence of the solution on the width of the diffuse interface $\eta$. If a model formulation introduces a model error, we still expect convergence toward the analytical solution for a finer mesh resolution as $\eta$ converges toward a small value with respect to the physical problem (i.e. $\eta/W \to 0$ which implies $\tilde{p}_{\text{PF}} \to 0$ at constant $\Delta f$). This can be easily tested by running the same simulation input parameters while changing the grid resolution and $\eta$, respectively. For this study, we choose driving forces of $\tilde{p} = \pm 10$, i.e. at the transition from intermediate to large driving forces. This ensures that the driving force

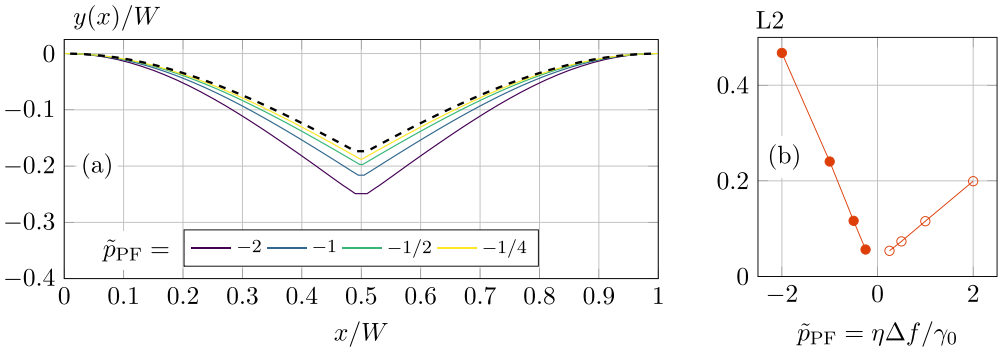


**Figure 6.** Interface-thickness convergence study of model $H1$ for varying $\eta$ at constant number of grid points in the interface ($n_{\mathrm{int}} = 10$) and constant physical width $W$. (a) Grain boundary geometries for $\tilde{p} = -10$ and grid spacings of $\Delta x \in \{1, 0.5, 0.25, 0.125\}\,\mu$m. The analytical GB profile is shown as a black dashed curve. (b) Deviation of the GB profile expressed in terms of L2 error for $\tilde{p} = -10$ (filled circles) and $\tilde{p} = 10$ (open circles).

is sufficiently large such that a change in interface thickness results in a measurable deviation (for small driving forces we do not expect significant deviations). In all current cases, the diffuse interface is discretized with 10 cells ($\eta = 10\Delta x$) which should keep the discretization error small and constant. For a constant physical domain size, we vary the interface thickness $\eta \in \{1.25, 2.5, 5, 10\}\,\mu$m to test convergence of the model. This corresponds to refined grids with $\Delta x \in \{0.125, 0.25, 0.5, 1\}\,\mu$m and $N_x \in \{400, 200, 100, 50\}$. The convergence of the grain boundary profile toward the analytical solution is illustrated for $\tilde{p} = -10$ and the model formulation $H1$ in figure 6(a). Note that the width of the diffuse interface is implicitly given by $\tilde{p}_{\mathrm{PF}}$ as defined in equation (2). Similar convergence was observed for the other model formulations (see section 6.2). This deviation from the analytical profile can be quantified by the L2 error norm defined in section 5 which is shown in figure 6(b).

Finer mesh resolution leads to a massive increase in computation time. For finite difference schemes on a regular grid, reducing $\Delta x$ by a factor of two results in a fourfold increase in grid cells in 2D. In addition, $\Delta t$ needs to be reduced by a factor of four when explicit time stepping is used, resulting in a 16 times increase in computation time. Therefore, an important question in the context of PF modeling is: Which model formulation allows maximum accuracy at low resolution of the diffuse interfaces?

### 6.2. *Model comparison*

We compare the MPF formulations given in section 4 by testing their model error with respect to the defined benchmark. As in the previous example, driving forces of $\tilde{p} = \pm 10$ are considered. We modify the interface thickness as in the previous subsection, keeping the number of cells in the interface constant at $n_{\mathrm{int}} = 10$ to test convergence of the model formulations. The results in figure 7(a) clearly show that even at the same interface thickness of $\eta = 5\,\mu$m (i.e. at $\tilde{p}_{\mathrm{PF}} = -1$), the model formulations perform differently. This becomes even more pronounced for increasing interface thickness as can be seen from the L2 geometry error in figure 7(b) and the relative velocity error in figure 7(c).

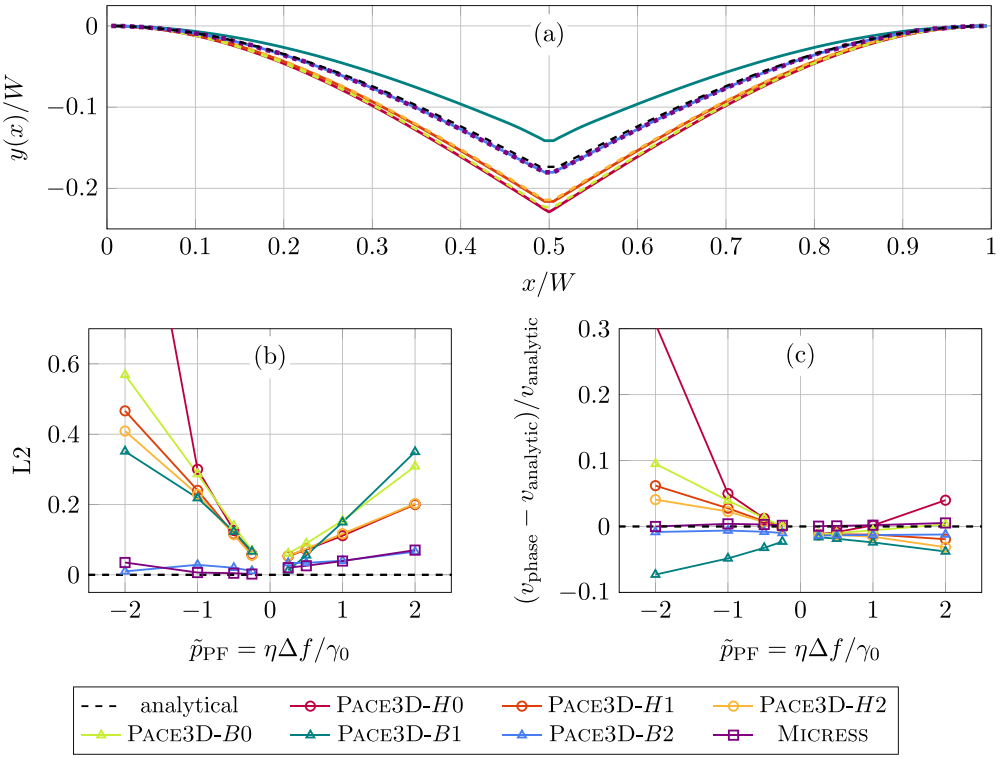


**Figure 7.** Performance of various model formulations. (a) Grain boundary geometry for $\tilde{p} = -10$ and $\tilde{p}_{\mathrm{PF}} = -1$ with the model formulations given in section 4. The analytical GB geometry is shown as a black dashed curve. (b) Deviation of the GB profile expressed in terms of relative L2 error for $\tilde{p} = \pm 10$ and (c) corresponding relative error of GB velocity.

Overall, there is a distinct model formulation $B2$ (i.e. equation (30)) which outperforms all others even at large interface thicknesses. For all mesh resolutions in this simulation study, the velocity error of $B2$ is below 1% for $\tilde{p} = -10$ and below 1.5% for $\tilde{p} = 10$. Additionally, as this formulation is implemented both in PACE3D and MICRESS, figure 7 includes results from two different implementations of this model. Since the error curves of both implementations nearly overlap, the two implementations yield very similar results. This indicates that both implementations correctly reflect equation (30) up to negligible deviations. Based on the results, model $B2$ seems to be a very efficient choice for practical applications. Therefore, we restrict the further investigations to this model formulation to discuss the effects of discretization and large driving forces.

### *6.3. Discretization error*

In the previous section which focused on model error, we aimed at minimizing the discretization error by using a high number of interface cells ($n_{\mathrm{int}} = 10$). In this section, in contrast, we minimize the model error by selecting model variant $B2$ and investigate the discretization error

that results from a reduced number of interface cells. We study this effect by fixing the interface width to $\eta = 2.5\,\mu$m while varying $\Delta x$ and, thus, the amount of interface cells. Note that low numbers of interface cells are essential to reduce computational costs in applied simulations. In this context, MICRESS uses a dedicated finite difference correction (FDC) that reduces the discretization error based on the work of Eiken [16]. In the following, we compare the geometry error and velocity error resulting from MICRESS simulations with and without FDC for various discretizations $\Delta x = \{0.625, 0.417, 0.315, 0.25\}\,\mu$m. The results in figures 8(c) and (d) show that, generally, the error increases when the diffuse interface is resolved with less grid points. The reduction of grid points leads to stronger numerical pinning which can be compensated by the FDC scheme as can be seen in figure 8(d). Even for a coarse interface resolution of four interface cells, the velocity error is below 1%.

### 6.4. Large driving forces

While the previous investigations were limited to $\tilde{p} = \pm 10$, we now investigate larger driving forces to cover a wide range of geometries. The first study, summarized in figure 9, is performed with MICRESS including FDC and a range of driving forces $\tilde{p} \in \{-80, -50, -10, 10, 50, 80\}$. For each driving force, simulations are performed with ten interface cells ($\eta = 10\Delta x$) but different resolution settings, i.e. $\Delta x \in \{1.0, 0.625, 0.5, 0.25, 0.125\}$ which in turn varies the PF specific driving force $\tilde{p}_{\mathrm{PF}}$. First of all, figure 9(a) reveals that large driving forces still pose a challenge for state-of-the art PF models since errors up to 100% in the GB-geometry are obtained. On the contrary, the relative error in the GB velocity shown in figure 9(b) is roughly an order of magnitude smaller. This shows that in contrast to the geometry, the predicted dynamics are more accurately reproduced and have a significantly smaller interface-thickness dependency. A peculiar feature is the very strong asymmetry in the velocity error with respect to a change of sign in driving force (and thus $\tilde{p}_{\mathrm{PF}}$). For positive driving forces, the error is negligible in comparison to the error for negative driving forces. We think that a possible explanation can be given as follows: For negative driving forces, the geometry is fully determined by the triple-junction angle (hat-like shape), whereas for positive driving forces (lid-like shape) the triple-junction slope $m$ has a negligible influence (cf figure 2). Considering that the vertical velocity is directly influenced by the slope of the GB according to equation (12), it is likely that the deviations are due to an incorrect dihedral angle $\theta$.

An important feature of figure 9 is that the error converges toward zero for $\tilde{p}_{\mathrm{PF}} \to 0$ in accordance with the results in section 6.2. Thus, reducing the interface thickness $\eta$ for a constant driving force improves the simulation accuracy for both the GB profile and velocity. For increasing driving forces $\Delta f$, the error can be kept almost constant by simultaneously decreasing the interface thickness $\eta$ by the same factor. This shows that larger driving forces require proportionally smaller interface widths in order to maintain the same level of accuracy and reveals an interesting fact: The error primarily depends on $\tilde{p}_{\mathrm{PF}}$ rather than on the dimensionless driving force $\tilde{p}$. This in turn means that the geometry of the GB, which varies strongly with $\tilde{p}$, has a subdominant influence on the total error. This result is remarkable as it suggests that the model error can be estimated for arbitrary scenarios such as polycrystalline setups, knowing only the interface thickness $\eta$, the involved driving force $\Delta f$ and the interfacial energies $\gamma$.

So far, the simulation studies were based on equal interfacial energies $\gamma_{\alpha\beta} = \gamma_0$ which results in a dihedral angle of $\theta = 120°$. For this combination, the junction term equation (29) vanishes. The analytical solution is general for arbitrary dihedral angles. In order to study a case significantly deviating from the simple case of $\theta = 120°$, we increase the energy of the

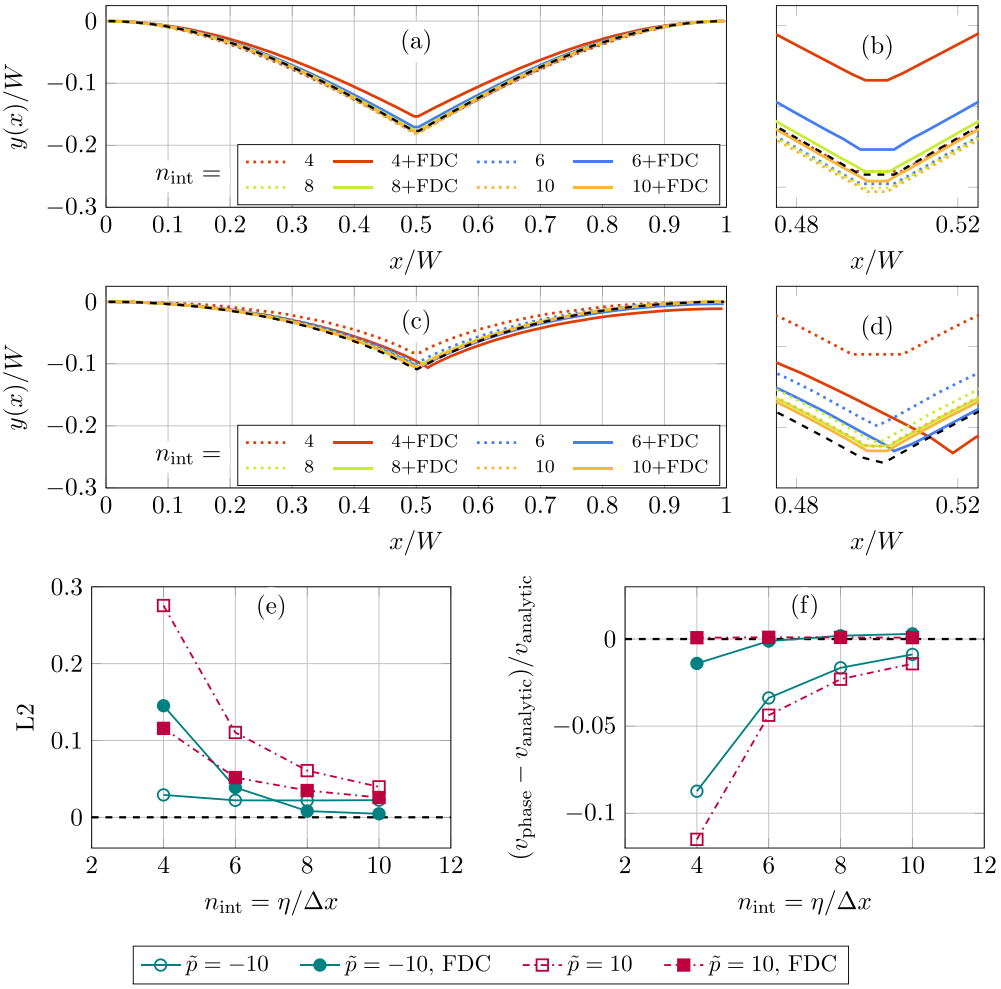


**Figure 8.** Quantification of discretization error for MICRESS-simulations. A fixed interface thickness $\eta = 2.5\,\mu$m and varying $n_{\text{int}} \in \{4, 6, 8, 10\}$ corresponding to $\Delta x = \{0.625, 0.417, 0.315, 0.25\}\,\mu$m are considered. GB profiles and magnification of triple-junction region for (a)/(b) $\tilde{p} = -10$ and (c)/(d) $\tilde{p} = 10$. Deviation of the GB profile expressed in terms of L2 error for $\tilde{p} = \pm 10$ (e) and corresponding relative error of GB velocity (f).

vertical GB by a factor $\gamma_{\alpha\beta} = \sqrt{3}\gamma_0$ which corresponds to $\theta = 60°$ according to equation (6). Figure 10 compares the FDC in MICRESS and the standard discretization used in PACE3D.

For negative driving forces, the geometry error of the FD-correction and the standard scheme are of a similar magnitude as for the 120° case with FDC. Here, the PACE3D code slightly outperforms MICRESS with respect to the measured errors in the GB geometry and velocity. However, for positive driving forces, the FD-correction implemented in MICRESS seems to give very accurate results both with respect to the geometry and velocity of the GB. This level of accuracy cannot be achieved with a standard numerical scheme in PACE3D. It is worth noting that despite the high resolution of $n_{\text{int}} = 10$, significant differences exist between

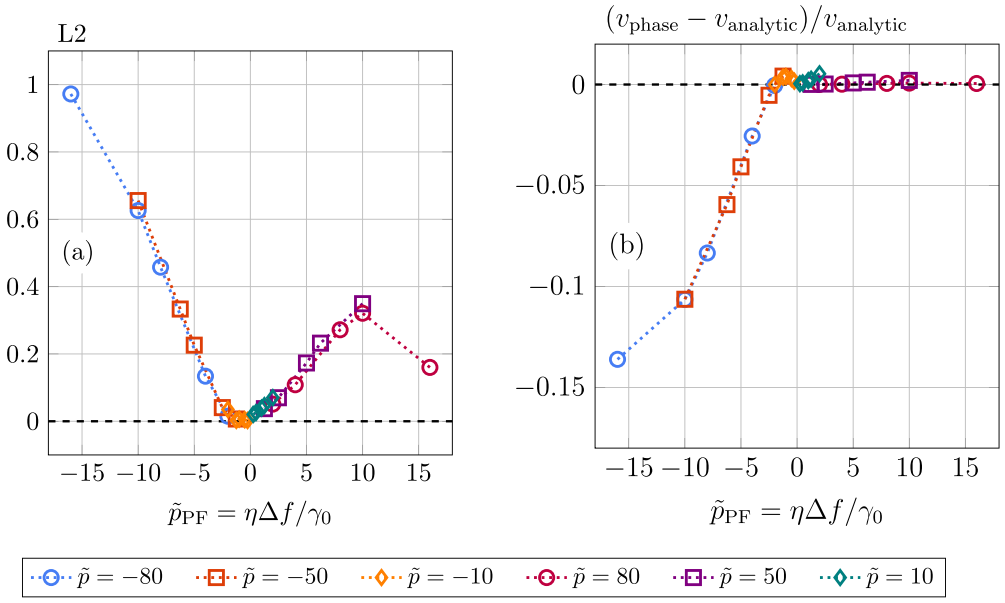


**Figure 9.** Comparison of geometry and velocity error in MICRESS-FDC for large driving forces. (a) Deviation of GB profile in terms of L2 error, (b) relative error of velocities. All simulations have been performed with model *B*2, $\eta = 10\Delta x$ and including finite difference correction.

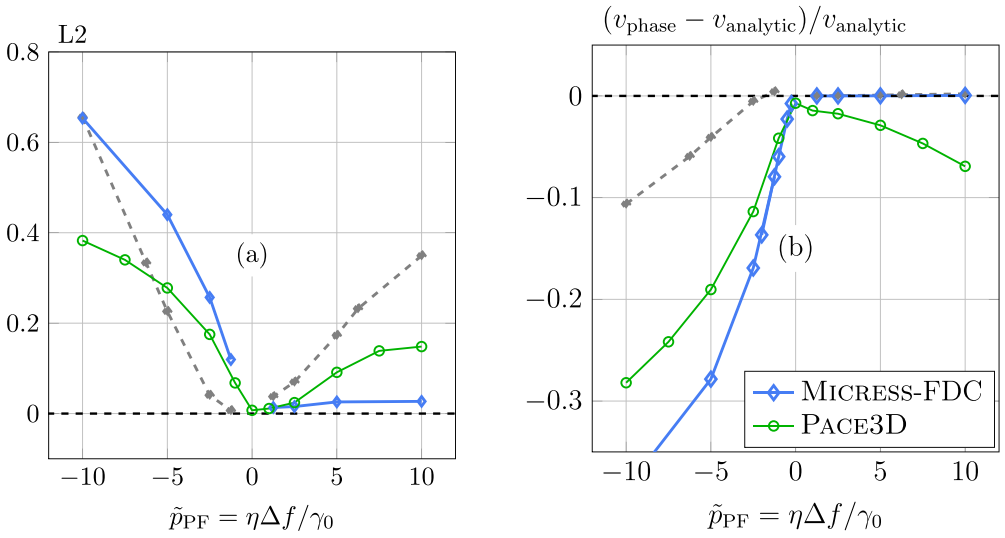


**Figure 10.** Large driving force study for $\theta = 60°$. (a) Deviation of GB profile in terms of L2 error, (b) relative error of velocities. Blue lines corresponds to MICRESS with FDC and green line corresponds to PACE3D (without FDC). All simulations are with $\eta = 10\Delta x$. Gray dashed lines show the result for $\theta = 120°$ from figure 9 for comparison.

the two numerical schemes at large driving forces. Without further proof, we think that this is rooted in the high absolute velocities of the GB which imply a high cell-Péclet number

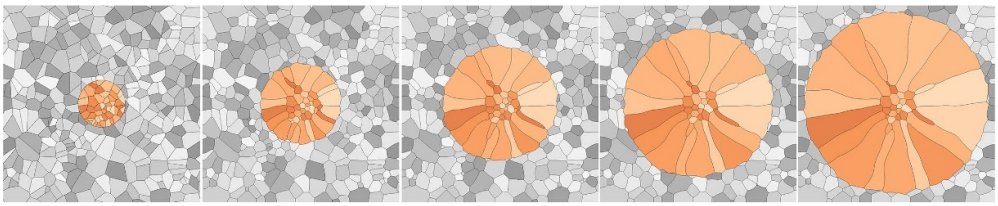

**Figure 11.** Temporal evolution of a polycrystalline system. The orange grain population grows due to a positive constant driving force while at the same time all grains coarsen to reduce interfacial energy. The physical domain is $250 \times 250\,\mu$m, other simulation parameters are taken from table 1.

$V\Delta x/(M_0\gamma_0) \propto \Delta f \Delta x/\gamma_0$ and thus seem to pose a challenge for the numerical schemes at a finite resolution.

### 6.5. *Polycrystalline sample subjected to large driving forces*

In the final simulation study, we investigate whether the conclusions from the triple junction benchmark can be transferred to arbitrarily complex polycrystalline systems. For this purpose, we study a population of grains growing into another polycrystalline domain as shown in figure 11. The orange grains exhibit a constant positive driving force of $\Delta f = 1$ MPa and the domain size equals $250\,\mu$m $\times$ $250\,\mu$m. The other simulation parameters are taken from table 1 as $\gamma_{\alpha\beta} = 0.5\,\mathrm{J\,m^{-1}}$ and $M = 2 \times 10^{-8}\,\mathrm{m^4\,(Js)^{-1}}$. The initial grain structure is generated based on a randomized seed creation followed by a Voronoi tesselation. To the best of our knowledge it is not possible to derive an exact analytical solution for this case, so we perform a classical mesh convergence study where we reduce $\Delta x$ by factors of two while keeping the amount of grid points in the diffuse interface constant $n_{\mathrm{int}} = 10$ (i.e. $\eta = 10\Delta x$).

Starting from the same initial setup, the phase evolution is first computed with PACE3D for model formulations B0-B2 and grid resolutions of $500^2$, $1000^2$, $2000^2$ and $4000^2$. Based on the results of the triple junction benchmark in section 6.2 we expect that all models converge towards a similar microstructure with refined resolution, but model B2 should converge significantly faster. From the results in figures 9 and 10, we also expect that all model formulations exhibit a velocity error $>5\%$ for values of $\tilde{p}_{\mathrm{PF}} > 5$. The visual comparison of the grain structure for $t = 3$ ms in figure 12 reveals that formulation B0 leads to a faster growth while B1 leads to a slower growth compared to model variant B2. This is consistent with the results in section 6.2. Furthermore, all models seem to converge towards the same microstructure evolution as $\tilde{p}_{\mathrm{PF}}$ becomes smaller. The two finest resolutions of model B2 yield almost identical results which is a hint for mesh convergence.

To quantify the simulation results, we evaluate an effective radius $R(t) = \sqrt{A(t)/\pi}$ from the area $A$ of the orange grain population. Figure 13(a) shows the radial velocity $\partial R/\partial t$ for the different model variants and numerical resolutions. As the number of grid points is increased, the different model formulations converge towards the same radial velocity. While the solution still changes for models B0 and B1 when going from a grid resolution of 2000–4000, the model formulation B2 is already converged at 2000 cells. Therefore, we take the simulation with B2 at the finest resolution as a reference to compute the relative deviation of $\partial R/\partial t$ which is shown in figure 13(c). There is little variation in computation times between the different model variants at constant resolution. However, each doubling of the resolution leads to a 10–16 fold increase in computation time. A factor of 16 is expected for a regular grid (4-fold increase in number

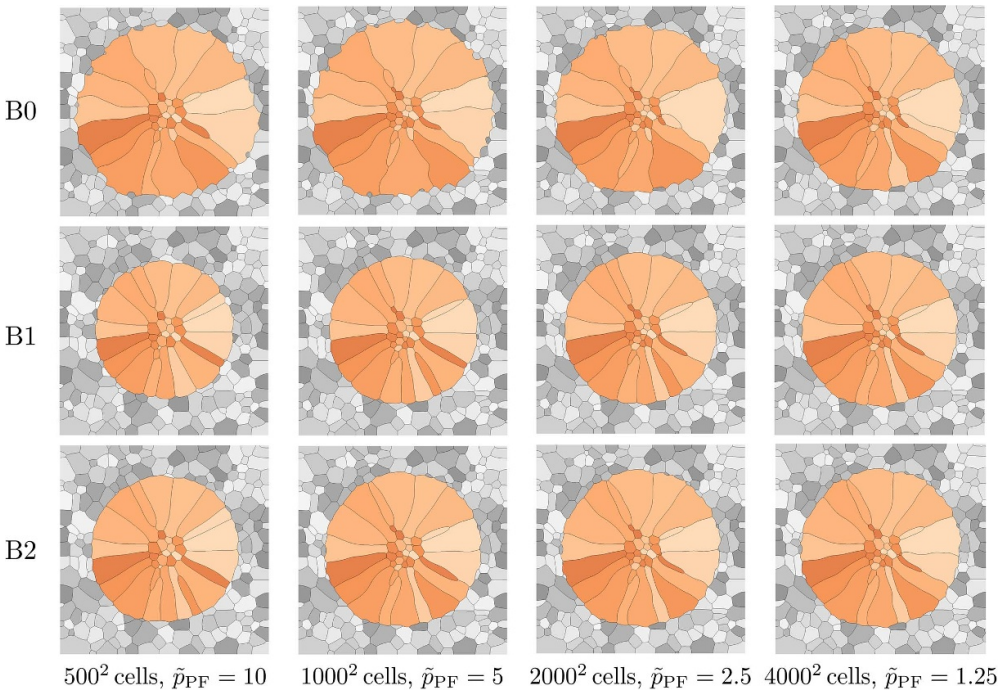


**Figure 12.** Grain structure at same point in time $t = 3$ ms computed with model formulations B0-B2 implemented in PACE3D at various grid resolutions.

of cells) and explicit time-stepping (4× smaller time step) which can be mitigated by the fact that for the obstacle potential all computations in bulk cells (where $\phi_\alpha = 1.0$, $\phi_\beta = 0\ \forall \beta \neq \alpha$ and $\boldsymbol{\nabla}\phi_\alpha = 0\ \forall \alpha$) can be skipped.

For a given accuracy limit of e.g. <5% deviation in the velocity as marked by the gray shaded area in figure 13(c), model B0 requires a resolution of $4000^2$ cells ($\tilde{p}_{\mathrm{PF}} = 1.25$) which comes at the computational cost of $t_{\mathrm{wall}} = 4580$ s. Meanwhile, model B1 requires a resolution of at least $2000^2$ cells ($\tilde{p}_{\mathrm{PF}} = 2.5$) while for model B2 a resolution of $1000^2$ cells ($\tilde{p}_{\mathrm{PF}} = 5$) would be sufficient. The resulting simulation time for B2 was 40.6 s which corresponds to a reduction of computational time by a factor of 113 compared to model B0.

Finally, we compute the same polycrystalline system with MICRESS and vary the amount of interface grid points, namely $n_{\mathrm{int}} = 5$ and $n_{\mathrm{int}} = 10$. The predicted grain structures in figure 14(a) are almost identical to the simulated results with PACE3D at high resolution. However, it is important to note that the prediction of polycrystalline grain evolution is not necessarily unique, as for the dissociation of a quadruple junction into two triple junctions two equivalent topological solutions exist. For a more quantitative comparison, the relative deviation of effective radial velocity is plotted in figure 14(b), taking the MICRESS simulation with highest resolution and 10 interface cells as a reference. The evaluation confirms that the converged MICRESS and PACE3D predictions are in good agreement, while the FDC in MICRESS [20] allows for enhanced accuracy even at reduced numerical resolution and a reduced number of interface cells. In summary, this example demonstrates that all conclusions from the simple triple junction benchmark hold true for the more complex polycrystalline sample.

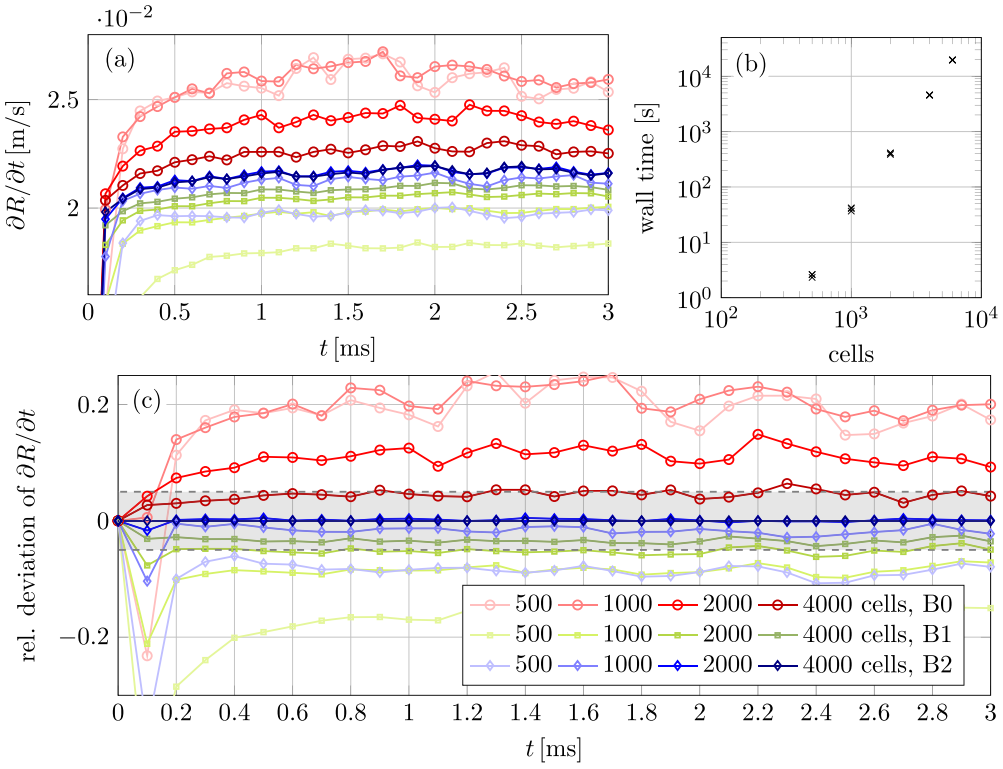


**Figure 13.** Comparison of model performance at various grid resolutions (a) given in terms of radial velocity, (b) wall time and (c) relative deviation of radial velocity with respect to converged solution (model B2 at $4000^2$ cells).

Furthermore, the results highlight the dramatic impact of the model formulation on the simulation accuracy, and consequently, on the computational time required to achieve a given level of accuracy.

## 7. Conclusion and outlook

A benchmark is presented for GB migration under the combined action of capillary and bulk driving forces. The benchmark consists of a three-phase setup for which an analytical steady-state solution is derived. The solution is kept general for arbitrary driving forces and dihedral angles.

We compare the analytical solution to PF simulations in a fully automated manner using well-defined metrics such as the relative L2 error of the GB geometry and the relative error in the interface velocity. The comparative study covers many different MPF models and two different numerical implementations, namely Pace3D and Micress. The post-processing framework, written in the Python programming language, is made available as open source software. This facilitates reproducibility of the results and allows a direct comparison with other models in the future. An interfacial thickness study shows that although all model variants seem to converge to the same sharp-interface limit, the model accuracy at a finite interfacial thickness

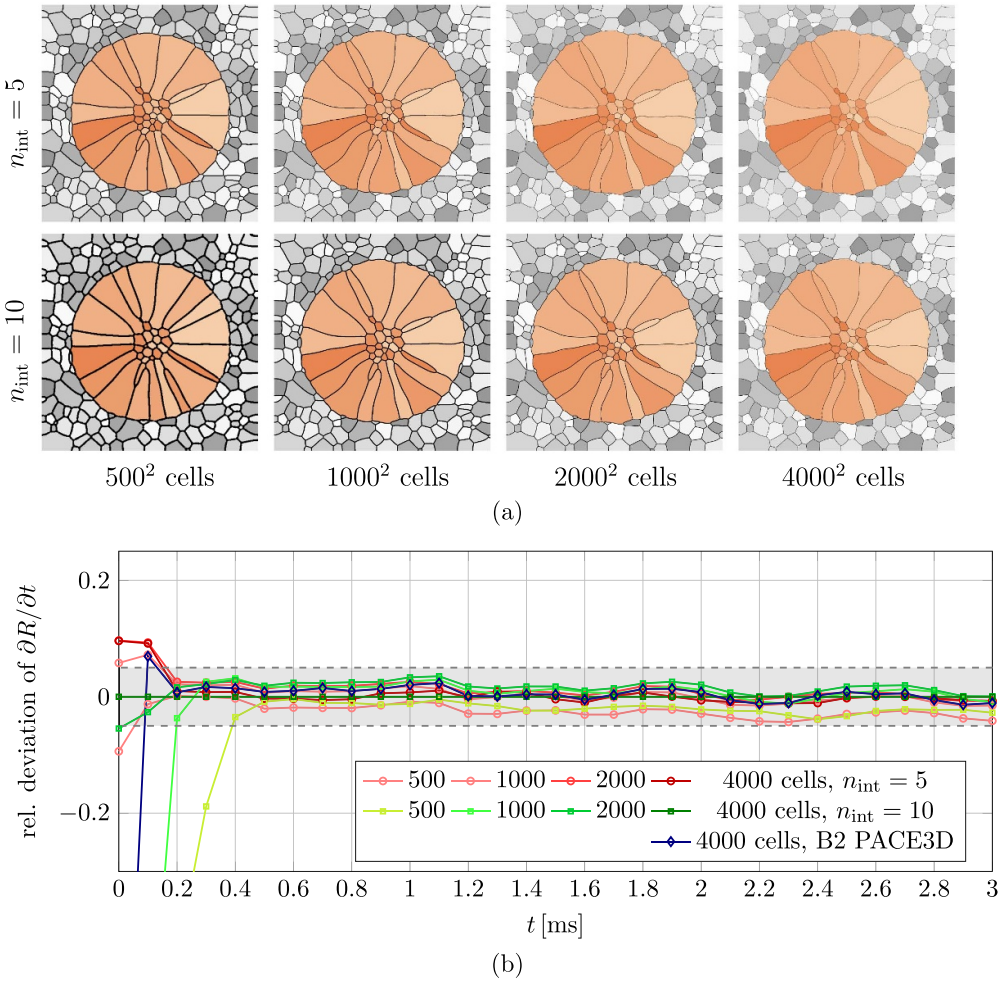


**Figure 14.** Polycrystalline simulation with MICRESS at various grid resolutions with $n_{\mathrm{int}} = 5$ and $n_{\mathrm{int}} = 10$ interface cells. (a) Grain structure at $t = 3$ ms and (b) relative deviation of radial velocity. The simulation with highest resolution ($4000^2$ cells, $n_{\mathrm{int}} = 10$) is taken as a reference.

can be substantially different. The error typically increases strongly with the ratio of the absolute bulk driving force to the interface stabilizing force, here denoted as $|\tilde{p}_{\mathrm{PF}}|$. Based on these results, a model formulation is identified that achieves superior performance with respect to all other formulations. This model formulation is then further investigated. An additional convergence study reveals the error introduced by a finite grid spacing and allows to identify the resolution required to achieve a given accuracy goal. Two different discretization schemes are compared: A standard finite-difference scheme and the correction introduced in [20] which is implemented in MICRESS. The latter approach yields a much higher accuracy in most of the cases, demonstrating its efficiency. A related approach, the so-called *sharp PF method* [17] has also recently been applied to grain growth [18]. It would be interesting to benchmark this model, the formulation from [25, 26] as well as other new approaches [14, 27, 28]

with the proposed framework in order to assess their efficiency and suitability for large driving forces. The results of the final simulation study underline the generality of the proposed benchmark as all predictions derived from the triple junction setup are observed as well in the polycrystalline case. This means that once a model formulation has been benchmarked using the analytical triple junction example, the model error can be predicted purely based on the PF specific driving force $\tilde{p}_{\mathrm{PF}}$. This procedure increases the reliability of MPF studies while making time-consuming convergence studies redundant.

In general, the current work shows how sensitive simulation results are with respect to slight modifications of PF models (e.g. all variations based on equation (27) only differ in a single prefactor but show completely different accuracy (cf figure 7)). There are many different model formulations in the literature based on a large number of possible combinations of energetic terms. It is concluded that any newly proposed model, even if it consists of a novel combination of existing terms, should be benchmarked before application.

## Data availability statement

Simulation studies were performed using the software packages Pace3D and Micress. Software licences for Pace3D in individually compiled form and optimised for specific applications can be purchased from the Steinbeis Transfer Centre 'Materials Simulation and Process Optimisation (stw1272)' [42]. Micress is commercially available on www.micress.de. The post-processing framework, written in the Python programming language, is made available as open source software on github [33].

We have added a data availability section which links to the openly available post-processing code and also refers to the commercial simulation codes used in this study. The data that support the findings of this study are available upon reasonable request from the authors.

## Acknowledgments

This work contributes to the research performed at CELEST (Center for Electrochemical Energy Storage Ulm-Karlsruhe) and was funded by the German Research Foundation (DFG) under Project ID 390874152 (POLiS Cluster of Excellence). Furthermore, funding by the Helmholtz association through the MSE Programme No. 43.31.01 is gratefully acknowledged, as well as funding via DFG under Project ID 467256728.

## Appendix A. Sharp-interface steady-state solution

### *A.1. General solution*

Equation (21) can be solved using integration by substitution. We first separate the variables by dividing through the right-hand side which gives

$$\frac{\tilde{y}''(\tilde{x})}{\tilde{v}\left(1+(\tilde{y}'(\tilde{x}))^2\right)-\tilde{p}\left(1+(\tilde{y}'(\tilde{x}))^2\right)^{3/2}}=1\,. \tag{A.1}$$

**Table A1.** Limiting interface velocities for certain special relations $q = \tilde{v}/\tilde{p}$.

| $q$ | $\tilde{v}$ | $\tilde{p}$ |
|---|---|---|
| $-\sqrt{1+m^2}$ | $\ln\left(1+m^2\right)/m - 2\arctan(m)$ | $-\tilde{v}/\sqrt{1+m^2}$ |
| $-1$ | $2\left(\left(\sqrt{1+m^2}-1\right)/m - \arctan(m)\right)$ | $-\tilde{v}$ |
| $0$ | $0$ | $2m/\sqrt{1+m^2}$ |
| $\sqrt{1+m^2}$ | $-\infty$ | $-\infty$ |
| $1$ | $\infty$ | $\infty$ |
| $\pm\infty$ | $-2\arctan(m)$ | $0$ |

Integrating with respect to $\tilde{x}$ and substituting $\tilde{y}'(\tilde{x}) \equiv s(\tilde{x})$ yields

$$\int_{s(0)}^{s(\tilde{x})} \frac{1}{\tilde{v}\left(1+s^2\right) - \tilde{p}\left(1+s^2\right)^{3/2}} \mathrm{d}s = \tilde{x}\,. \tag{A.2}$$

We use WolframAlpha [43] to perform the integral on the left-hand side. This gives

$$\begin{aligned}\frac{\arctan(s)}{\tilde{v}} + \frac{\tilde{p}}{\tilde{v}\sqrt{\tilde{v}^2-\tilde{p}^2}}\left(\operatorname{arctanh}\left(\frac{s\tilde{v}}{\sqrt{1+s^2}\sqrt{\tilde{v}^2-\tilde{p}^2}}\right)\right.\\ \left.+\operatorname{arctanh}\left(\frac{s\tilde{p}}{\sqrt{\tilde{v}^2-\tilde{p}^2}}\right)\right) = \tilde{x}+\tilde{x}_0\end{aligned} \tag{A.3}$$

where $\tilde{x}_0$ is an integration constant. The boundary condition at the mirror plane (equation (23)) requires $\tilde{x}_0 = 0$. The second boundary condition (equation (24)) gives an expression relating the GB velocity to the driving force:

$$\begin{aligned}\frac{\tilde{p}}{\tilde{v}\sqrt{\tilde{p}^2-\tilde{v}^2}}\left(\arctan\left(\frac{m\tilde{v}}{\sqrt{1+m^2}\sqrt{\tilde{p}^2-\tilde{v}^2}}\right)+\arctan\left(\frac{m\tilde{p}}{\sqrt{\tilde{p}^2-\tilde{v}^2}}\right)\right)\\ -\frac{\arctan(m)}{\tilde{v}} = \frac{1}{2}\,.\end{aligned} \tag{A.4}$$

Solving for $\tilde{v}$ for a given driving force $\tilde{p}$ therefore turns into a rootfinding problem. There exist special relations $q = \tilde{v}/\tilde{p}$ for which $\tilde{v}$ can be directly obtained by a limit from the equivalent expression in equation (25). These are tabulated in table A1. We derive lower and upper bounds for $\tilde{v}$ under the assumption that $\tilde{v}$ increases monotonously with $\tilde{p}$ [6]. Starting from these bounds, we then apply a bracketing algorithm implemented in SciPy according to [44] in order to solve equation (A.4) for $\tilde{v}$. This routine usually converges within a small number of iterations to reach the desired numerical accuracy. The applied lower and upper bounds are tabulated in table A2.

After solving for $\tilde{v}$, the solution $\tilde{y}(\tilde{x})$ is numerically computed by first selecting a finite number of slopes $s$ between $-m$ and $m$ and computing the corresponding coordinate $\tilde{x}$ using equation (A.3). Thereafter, composite trapezoidal rule is used to compute a numerical approximation to $\tilde{y}(\tilde{x})$. This procedure is repeated for a number of grid refinements (w.r.t. $s$) until a certain relative $L^2$-error between the coarse and fine solution is reached.

[6] Proving this seems not to be straightforward, but we think this is a reasonable assumption since an increase in driving force should result in an increase of the velocity in the same direction.

**Table A2.** Derived lower and upper bounds for the dimensionless interface velocity depending on the driving force. The criticial driving forces are given by $\tilde{p}_1 = (2\arctan(m) - \ln(1+m^2)/m)/\sqrt{1+m^2}$, $\tilde{p}_2 = 2(\arctan(m) + (1-\sqrt{1+m^2})/m)$ and $\tilde{p}_{\text{stat}} = 2m/\sqrt{1+m^2}$. The bounds rest on the limits tabulated in table A1 and the bounds for negative $\tilde{p}$ are derived as detailed in the supplementary material.

| $\tilde{p}$-Interval | Lower Bound ($\tilde{v}$) | Upper Bound ($\tilde{v}$) |
|---|---|---|
| $-\infty < \tilde{p} < 0$ | $\min(-6\arctan(m), -\sqrt{(1+m^2)\tilde{p}^2 + 6m\lvert\tilde{p}\rvert})$ | $\min(-2\arctan(m), \sqrt{1+m^2}\tilde{p})$ |
| $0 < \tilde{p} < \tilde{p}_1$ | $-2\arctan(m)$ | $\ln(1+m^2)/m - 2\arctan(m)$ |
| $\tilde{p}_1 < \tilde{p} < \tilde{p}_2$ | $\ln(1+m^2)/m - 2\arctan(m)$ | $2((\sqrt{1+m^2}-1)/m - \arctan(m))$ |
| $\tilde{p}_2 < \tilde{p} < \tilde{p}_{\text{stat}}$ | $2((\sqrt{1+m^2}-1)/m - \arctan(m))$ | 0 |
| $\tilde{p}_{\text{stat}} < \tilde{p} < \infty$ | 0 | $\tilde{p}$ |

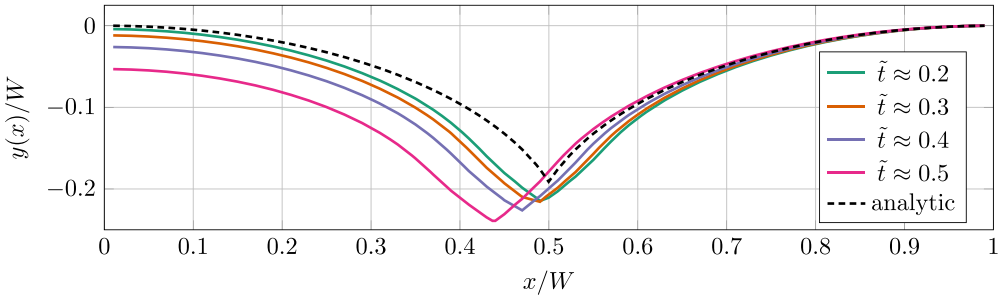


**Figure B1.** Instable GB evolution observed for variant PACE3D-*B*1 and $\theta = 60°$ at a driving force of $\tilde{p} = 10$.

## Appendix B. Instabilities

Although most of the simulations reach a steady-state configuration that is symmetric with respect to $x = W/2$, some cases develop an asymmetry that is either small (figure 8(d)) or large and growing significantly with time (cf figure B1). This reveals a clear limitation of the benchmark—the vertical GB tends to move horizontally as soon as a perturbation (e.g. due to round-off errors) exists which in turn may lead to a violation of the assumed symmetry. We have observed such cases rarely and only for $\tilde{p} > 0$. It is worth stressing that this may complicate the application of the benchmark in certain practical cases. In PF models, a strategy which might help suppressing this effect is to reduce the mobility of the vertical GB (i.e. $M_{\alpha\beta}$) which hinders its movement. However, this might induce an additional pinning effect according to Nani and Nestler [45] depending on which formulation is used. It should be noted that violation of the symmetry is an artificial effect which only exists due the simplified setup, which is absent in most if not all real polycrystalline scenarios. Therefore, without further proof, we consider it as a limitation of the benchmark rather than the model implementation.

## ORCID iD

P W Hoffrogge https://orcid.org/0000-0002-2332-6033

## References


[1] Steinbach I and Pezzolla F 1999 A generalized field method for multiphase transformations using interface fields *Physica* D **134** 385–93
[2] Nestler B, Garcke H and Stinner B 2005 Multicomponent alloy solidification: phase-field modeling and simulations *Phys. Rev.* E **71** 041609
[3] Eiken J, Böttger B and Steinbach I 2006 Multiphase-field approach for multicomponent alloys with extrapolation scheme for numerical application *Phys. Rev.* E **73** 066122
[4] Herring C 1951 Some theorems on the free energies of crystal surfaces *Phys. Rev.* **82** 87–93
[5] Young T 1805 III. An essay on the cohesion of fluids *Phil. Trans. R. Soc.* **95** 65–87
[6] Gottstein G, King A H and Shvindlerman L S 2000 The effect of triple-junction drag on grain growth *Acta Mater.* **48** 397–403
[7] Barrales Mora L A, Mohles V, Shvindlerman L S and Gottstein G 2008 Effect of a finite quadruple junction mobility on grain microstructure evolution: theory and simulation *Acta Mater.* **56** 1151–64
[8] Mießen C, Liesenjohann M, Barrales-Mora L A, Shvindlerman L S and Gottstein G 2015 An advanced level set approach to grain growth—accounting for grain boundary anisotropy and finite triple junction mobility *Acta Mater.* **99** 39–48
[9] Gottstein G and Shvindlerman L S 2009 *Grain Boundary Migration in Metals* vol 31, 2nd edn (CRC Press)
[10] Krill C E, Helfen L, Michels D, Natter H, Fitch A, Masson O and Birringer R 2001 Size-dependent grain-growth kinetics observed in nanocrystalline Fe *Phys. Rev. Lett.* **86** 842–5
[11] Gleiter H 1982 On the structure of grain boundaries in metals *Mater. Sci. Eng.* **52** 91–131
[12] Wang F and Nestler B 2024 Wetting and contact-angle hysteresis: density asymmetry and van der Waals force *Phys. Rev. Lett.* **132** 126202
[13] Hoffrogge P W and Barrales-Mora L A 2017 Grain-resolved kinetics and rotation during grain growth of nanocrystalline aluminium by molecular dynamics *Comput. Mater. Sci.* **128** 207–22
[14] Grose C J and Asimow P D 2022 A multi-phase field model for mesoscopic interface dynamics with large bulk driving forces *Comput. Mater. Sci.* **212** 111570
[15] Karma A 2001 Phase-field formulation for quantitative modeling of alloy solidification *Phys. Rev. Lett.* **87** 115701
[16] Eiken J 2012 Numerical solution of the phase-field equation with minimized discretization error *IOP Conf. Ser.: Mater. Sci. Eng.* **33** 012105
[17] Finel A, Le Bouar Y, Dabas B, Appolaire B, Yamada Y and Mohri T 2018 Sharp phase field method *Phys. Rev. Lett.* **121** 025501
[18] Dimokrati A, Le Bouar Y, Benyoucef M and Finel A 2020 S-PFM model for ideal grain growth *Acta Mater.* **201** 147–57
[19] Daubner S, Hoffrogge P W, Minar M and Nestler B 2023 Triple junction benchmark for multiphase-field and multi-order parameter models *Comput. Mater. Sci.* **219** 111995
[20] Eiken J 2020 Discussion of the accuracy of the multi-phase-field approach to simulate grain growth with anisotropic grain boundary properties *ISIJ Int.* **60** 1832–4
[21] Staublin P, Mukherjee A, Warren J A and Voorhees P W 2022 Phase-field model for anisotropic grain growth *Acta Mater.* **237** 118169
[22] Mullins W W 1956 Two-dimensional motion of idealized grain boundaries *J. Appl. Phys.* **27** 900–4
[23] Takaki T, Hisakuni Y, Hirouchi T, Yamanaka A and Tomita Y 2009 Multi-phase-field simulations for dynamic recrystallization *Comput. Mater. Sci.* **45** 881–8
[24] Kellner M, Sprenger I, Steinmetz P, Hötzer J, Nestler B and Heilmaier M 2017 Phase-field simulation of the microstructure evolution in the eutectic NiAl-34Cr system *Comput. Mater. Sci.* **128** 379–87
[25] Schoof E, Schneider D, Streichhan N, Mittnacht T, Selzer M and Nestler B 2018 Multiphase-field modeling of martensitic phase transformation in a dual-phase microstructure *Int. J. Solids Struct.* **134** 181–94
[26] Sun Y and Beckermann C 2007 Sharp interface tracking using the phase-field equation *J. Comput. Phys.* **220** 626–53
[27] Feyen V and Moelans N 2023 Quantitative high driving force phase-field model for multi-grain structures *Acta Mater.* **256** 119087
[28] Zhang J, Chadwick A F, Chopp D L and Voorhees P W 2023 Phase field modeling with large driving forces *npj Comput. Mater.* **9** 166

[29] Moelans N, Wendler F and Nestler B 2009 Comparative study of two phase-field models for grain growth *Comput. Mater. Sci.* **46** 479–90
[30] Miyoshi E, Takaki T, Ohno M and Shibuta Y 2020 Accuracy evaluation of phase-field models for grain growth simulation with anisotropic grain boundary properties *ISIJ Int.* **60** 160–7
[31] Turnbull D 1951 Theory of grain boundary migration rates *JOM* **3** 661–5
[32] Cahn J W and Taylor J E 1994 Surface motion by surface diffusion *Acta Metall. Mater.* **42** 1045–63
[33] TriplePy—post-processing code for the triple junction benchmark (available at: https://github.com/triple-junction/triplepy)
[34] Apel M, Eiken J and Hecht U 2014 Phase field models for heterogeneous nucleation: application to inoculation in alpha-solidifying Ti-Al-B alloys *Eur. Phys. J. Spec. Top.* **223** 545–58
[35] Kubendran Amos P G, Schoof E, Schneider D and Nestler B 2018 Chemo-elastic phase-field simulation of the cooperative growth of mutually-accommodating Widmanstätten plates *J. Alloys Compd.* **767** 1141–54
[36] Eiken J 2010 Phase-field simulation of microstructure formation in technical magnesium alloys *Int. J. Mater. Res.* **101** 503–9
[37] Eiken J, Böttger B and Apel M 2023 Diffuse modelling of pearlite growth in Calphad-coupled multicomponent multi-phase-field simulations *IOP Conf. Ser.: Mater. Sci. Eng.* **1281** 012051
[38] Steinbach I, Pezzolla F, Nestler B, Seeßelberg M, Prieler R, Schmitz G J and Rezende J L L 1996 A phase field concept for multiphase systems *Physica* D **94** 135–47
[39] Hötzer J, Reiter A, Hierl H, Steinmetz P, Selzer M and Nestler B 2018 The parallel multi-physics phase-field framework PACE3D *J. Comput. Sci.* **26** 1–12
[40] Hötzer J, Tschukin O, Said M B, Berghoff M, Jainta M, Barthelemy G, Smorchkov N, Schneider D, Selzer M and Nestler B 2016 Calibration of a multi-phase field model with quantitative angle measurement *J. Mater. Sci.* **51** 1788–97
[41] Minar M and Moelans N 2022 Benchmarking of different strategies to include anisotropy in a curvature-driven multi-phase-field model *Phys. Rev. Mater.* **6** 103404
[42] Steinbeis-Transferzentrum Werkstoffsimulation und Prozessoptimierung (available at: www.steinbeis.de/de/verbund/suche-im-steinbeis-verbund/detail.html?tx_z7suprofiles_detail%5Bprofile%5D=1911&cHash=6a6be509095c2b2f079fa423f7e7144e)
[43] Integration performed with WolframAlpha (available at: www.wolframalpha.com/input?i=integral+1%2F%28v+%281%2Bs%5E2%29+-+p+Sqrt%281%2Bs%5E2%29%5E%283%29%29+ds)
[44] Bus J C P and Dekker T J 1975 Two efficient algorithms with guaranteed convergence for finding a zero of a function *ACM Trans. Math. Softw.* **1** 330–45
[45] Nani E S and Nestler B 2023 Asymptotic analysis of multi-phase-field models: a thorough consideration of junctions *Phys. Rev.* E **107** 1–21